CRYSTAL GROWTH & DESIGN

Article

pubs.acs.org/crystal

Large Single Crystal SnS_2 Flakes Synthesized from Coevaporation of Sn and S

Y.-B. Yang,*[,†] J. K. Dash,[†] A. J. Littlejohn,[†] Y. Xiang,[†] Y. Wang,[‡] J. Shi,[‡] L. H. Zhang,[§] K. Kisslinger,[§] T.-M. Lu,[†] and G.-C. Wang[†]

[†]Department of Physics, Applied Physics and Astronomy and [‡]Department of Materials Science and Engineering, Rensselaer Polytechnic Institute, 110 Eighth Street, Troy, New York 12180-3950, United States

[§]Center for Functional Nanomaterials, Brookhaven National Lab, Building 735, P.O. Box 5000, Upton, New York 11973, United States

ABSTRACT: Remarkable properties of layered metal dichalcogenides and their potential applications in various fields have raised intense interest worldwide. We report tens of microns-sized ultrathin single crystal SnS_2 flakes grown on amorphous substrates using a simple one-step thermal coevaporation process. X-ray pole figure analysis reveals that a majority of flakes are oriented with the (0001) plane parallel to the substrate and a preferred fiber texture. For few-layer-thick SnS_2, Moire patterns of 6-fold and 12-fold symmetries are observed by transmission electron microscopy imaging and diffraction. These patterns result from the relative rotation between SnS_2 layers in the ultrathin flake. The 12-fold symmetry is consistent with a known quasicrystal pattern. The photoluminescence spectrum supports that these ultrathin flakes possess a direct bandgap. Carrier lifetime measured by time-resolved photoluminescence of a single flake is a few nanoseconds. These results improve our understanding of the formation and shape of ultrathin SnS_2 flakes.

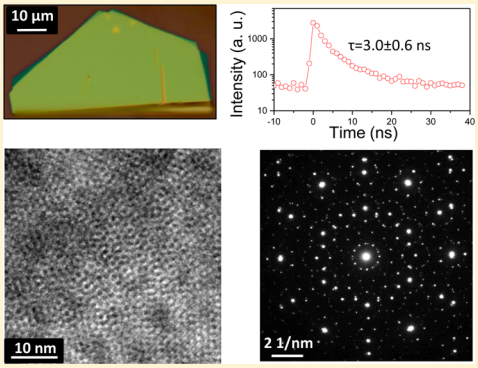

1. INTRODUCTION

Layered metal dichalcogenide (LMD) semiconductors such as MoS_2 and WS_2 have attracted intense interest recently due to their fundamental scientific importance and potential applications in electronics and optoelectronics. For example, strong photoluminescence (PL) emission from monolayer MoS_2 that is absent in the indirect bandgap bulk materials has been predicted by theory and observed experimentally,[1] and a single layer MoS_2 transistor has been demonstrated.[2] Among these LMD semiconductors, SnS_2 is less explored compared with MoS_2 or WS_2. However, reports of various synthesis methods, property characterizations, and potential applications have increased rapidly. Many characteristics which make SnS_2 a promising candidate for a variety of applications have been demonstrated including high carrier mobility,[3] high on−off current ratios in field effect transistors,[3−5] high optical absorption and photocatalytic activities,[6] fast photodetection response time,[7] and flexible photodetectors from UV to infrared.[8] Other potential applications such as a hybrid of SnS_2 with graphene[9,10] or with carbon nanospheres[11] or nanocomposite of SnS_2 with polyaniline[12,13] that exhibits high charge storage capacity, rate, stability, and long cycle life anodes for Li or Na ion batteries and a heterojunction of n-type SnS_2 with p-type BiOI semiconductor with enhanced visible light photocatalytic activity[11] have also been reported.

Various methods from simple to elaborate have been used to grow SnS_2 single crystals, nanostructures, and films. Examples include mechanical[3] and chemical exfoliations,[9] chemical vapor transport using iodine as the transport agent,[4,5] chemical vapor deposition (CVD)[14] using SnO_2,[7] atmospheric vapor pressure deposition using SnS_2,[15] hydrothermal,[11,13,16−20] wet chemistry,[21] solid state reaction,[22,23] atomic layer deposition,[24] solvothermal method,[25] and hot-injection method.[26] In this work we present a one-step method with a short turn-around time to grow single crystalline ultrathin (a few nanometers) to thin SnS_2 (hundreds of nanometers) flakes with diameters of over tens of microns on amorphous SiO_2 substrates: coevaporation of Sn at 600 °C and S at 150 °C under Ar flow on SiO_2 substrates held at 600 °C.

For SnS_2 to have potential applications as a window buffer layer in solar cells one needs to know the crystalline structure and stoichiometry of SnS_2. These can affect their optoelectronic properties. The crystallographic structure of a material determines the energy band structure which determines the density of states, bandgap, radiative transition energy, effective mass of charge carriers, and mobility. The texture and the finite crystalline size in a film break the long-range order and form, for example, grain boundaries that act as the recombination centers and can reduce the carrier lifetime. The inhomogeneity of chemical elements or impurities in a film serves as additional charge scattering centers or charge traps that further affect the charge transport and carrier lifetime. The carrier lifetime, for

Received: October 25, 2015
Revised: December 8, 2015

DOI: 10.1021/acs.cgd.5b01512
Cryst. Growth Des. XXXX, XXX, XXX−XXX

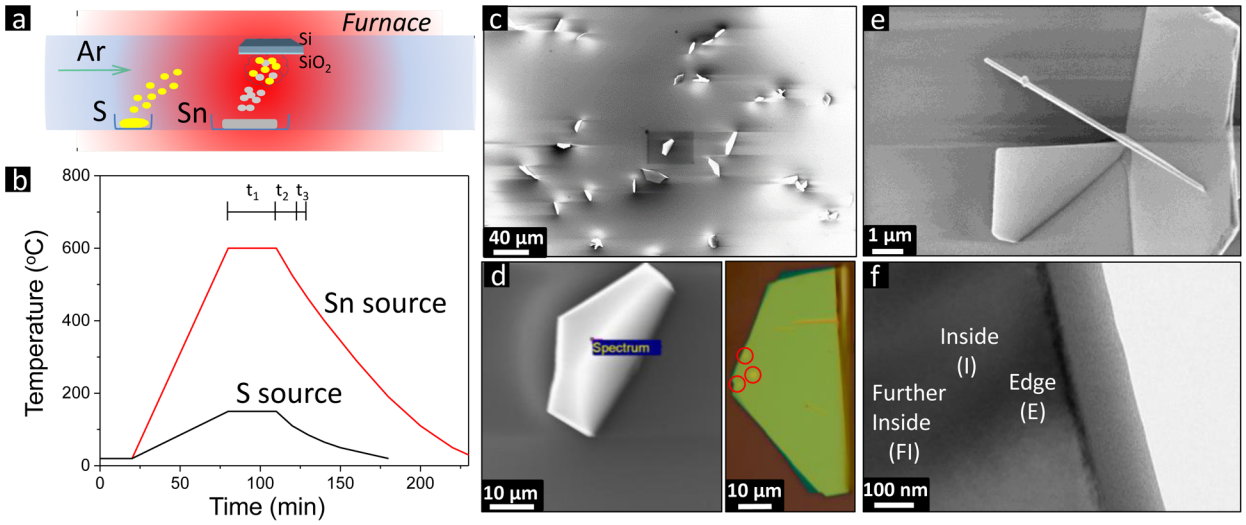

Figure 1. (a) Schematic (not to scale) of the experimental setup for the synthesis of SnS_2 flakes in a one zone furnace. The larger and smaller quartz boats contain Sn pellets and S powder, respectively. The SiO_2/Si(001) substrate faces downward. Thermocouple wires are placed near the center of the furnace. Argon gas flows from the S source to the Sn source as indicated. (b) Temperatures of S and Sn sources vs. time during the SnS_2 growth. t_1 denotes the time period during which the furnace is at the synthesis temperature of 600 °C. During t_2 and t_3 the temperature decreases gradually. Scanning electron microscopy top-view images of (c) many flakes, (d) one lying down flake, and (e) one vertical flake and three nonvertical flakes. The right panel of (d) shows an optical image of a flake. The three red circles contain islands to be analyzed by AFM. (f) TEM image of a flake after thinning by FIB. "E", "I", and "FI" stand for edge, inside, and further inside locations on a flake, respectively. The scale bars in (c–f) are 40 μm, 10 μm, 1 μm, and 100 nm, respectively.

example, is strongly related to the open-circuit voltage in the p–n junction of a solar cell. The morphology of a film affects the optical absorption, refraction, and scattering. The chemical inertness and stability affect the lifetime of a working device. We applied multiple characterization techniques to study the physical and chemical parameters of SnS_2 that can influence its optoelectronic properties.

We characterized the flakes' structure, orientation distribution, morphology, composition, and optical bandgap using X-ray diffraction (XRD), glancing incidence angle X-ray diffraction (GIXRD), X-ray pole figure analysis, reflection high energy electron diffraction (RHEED), transmission electron microscopy (TEM), scanning electron microscopy (SEM), energy dispersive X-ray analysis (EDX), X-ray photoelectron spectroscopy (XPS), atomic force microscopy (AFM), Raman spectroscopy, photoluminescence (PL), and time-resolved PL.

Several findings regarding the SnS_2 flakes synthesized using our simple method are reported here. (1) Flakes with lateral sizes of over tens of microns can be controlled by the relative amount of starting materials (solid Sn and solid S), and the synthesis time is short (<30 min). The method can be scaled up cost effectively. (2) The individual SnS_2 flakes are single crystal as revealed by RHEED and TEM diffraction. (3) The stoichiometry of SnS_2 is close to a 1:2 ratio as revealed by XPS and EDS. (4) From the X-ray pole figure analysis of the flakes across the entire sample, the preferred orientation is found to be [0001]. (5) For few-layer-thick flakes, Moire fringes and a quasicrystal pattern are formed as a result of a relative rotation between layers where weak van der Waals interaction governs. (6) The local bonding environment is uniform and the degree of crystallinity is high as reflected by the existence of only one Raman peak with a narrow full-width-at-half-maximum (fwhm). (7) A single PL peak is observed from more than one monolayer thick SnS_2 flakes implying a direct bandgap.

Our growth method involves the coevaporation of pure Sn pellets and sulfur powders onto a substrate. This differs from other large SnS_2 flake growth method using one-step CVD,[7,27] two-step CVD,[28] or atmospheric vapor deposition,[15] where the starting materials are either SnO_2 or SnS_2 powders. Their growth temperatures are higher than the 600 °C that we used. We applied X-ray pole analysis and RHEED patterns on these flakes. We learned the preferred texture of flakes, quantitative flake tilt angles with respect to the substrate, and in-plane rotation angle of vertical standing flake with respect to the substrate. These characteristics cannot be obtained from just X-ray theta vs two theta scan alone. From the TEM examination of a single flake, Moire fringes of superlattice and quasicrystal resulting from relative rotation of adjacent SnS_2 layers in the flake were observed for the first time. Furthermore, we explain the growth mode and shape of SnS_2 flakes through a detail analysis of AFM images.

2. EXPERIMENTAL SECTION

2.1. Synthesis Method for SnS_2 Flakes. SnS_2 flakes were synthesized by coevaporation of Sn and S on a 300 nm thick SiO_2/Si substrate in a quartz tube (30 in. long with outside/inside diameters of 59 mm/55 mm) inside a one zone furnace. The substrate was mounted upside down facing the Sn source. See the schematic in Figure 1a. The Sn pellets (99.99% purity, 0.8333 g) were placed in a quartz boat (100 × 45 × 20 mm) and positioned near the center of the furnace where the temperature is close to the preset temperature. The sulfur powder (99.98% purity, 2.3000 g) placed in a second quartz boat was positioned near the end of the quartz tube where the temperature is lower (~150 °C) than the preset temperature (600 °C). The quartz tube was purged with an ultrahigh purity (99.999%) grade Ar gas with a flow rate of 950 sccm from the side containing the sulfur boat to the side of the Sn boat and SiO_2/Si substrate. After 20 min of Ar gas purging, the Ar gas flow rate was reduced from 950 to 200 sccm, while the Sn, the substrate, and the S were gradually heated up to a preset temperature. See Figure 1b for the temperatures of Sn and S vs. time. With a ramping rate of 10 °C/min, it took about 60 min to raise the temperature from room temperature to 600 °C. The

DOI: 10.1021/acs.cgd.5b01512
Cryst. Growth Des. XXXX, XXX, XXX–XXX

temperature ramping was managed using a Eurotherm 2116 PID programmable temperature controller attached to the furnace. The temperature was measured using a type K thermocouple. The boat containing Sn was kept at 600 °C, while the sulfur containing boat near the end of furnace was at 150 °C. t_1 in Figure 1b indicates synthesized time period. After 30 min the furnace filament current was gradually reduced to zero over 5−6 min. The quartz tube was cooled down to room temperature in about 120 min. The initial cool down periods are labeled as t_2 and t_3. This slow cooling period has resulted in the island formation on flakes to be presented later. Argon gas purging was continuous during the entirety of the heating and cooling processes. Samples were prepared under these growth conditions three times, and results were reproduced. In addition, two variations from this procedure were studied. When the temperatures of Sn and the substrate were lowered from 600 to 580 °C, while keeping all other conditions the same, we did not observe the SnS_2 flakes on the substrate from X-ray diffraction, optical images, and AFM. When the growth temperature was raised from 600 to 650 °C and the amount of Sn pellets in the Sn boat was reduced, flakes were formed lying down flat on the substrate. However, the shapes of flakes were less regular (triangles, truncated triangles, hexagons, and other arbitrary shapes), and the flake sizes were smaller as compared to the SnS_2 flakes grown at 600 °C. These lying down flat flakes were not all connected. We believe that with more optimization work such as a longer growth time and a fine tone in temperature between 600 and 650 °C, a continuous film may be achieved. Robles et al.[29] have used coevaporation of Sn and S onto glass substrates and observed a mixture of SnS, SnS_2, and Sn_2S_3 phases in 700 nm thick or 1200 nm thick film. After postannealing the low deposition rate samples at 500 °C in the sulfur atmosphere, the SnS_2 phase dominated. If a sample was grown at a high deposition rate and postannealed at 500 °C in sulfur atmosphere, the mixed phase film progressed toward the SnS_2 phase. In both cases the film was SnS_2 dominant but still contained SnS and Sn_2S_3 phases, unlike our single phase SnS_2. In this paper we only report the detailed results of SnS_2 flakes grown at 600 °C.

2.2. Characterization Techniques Used. The surface morphologies of synthesized samples were imaged using a ZEISS SUPRA 55 FE scanning electron microscope (SEM) and a PSI XE100 AFM in contact mode. The Olympus-AC240TS AFM tip used has a tip radius of ∼7 nm, a force constant of 2 N/m, and a resonant frequency of 70 kHz. The chemical composition of flakes were measured using the EDS in the same SEM system.

XPS was used to measure the near surface composition of the sample. The nearly monochromatic X-ray Mg K source (PHI model 04-151) had a primary energy of 1253.6 eV. The operation conditions of the X-ray source are 270 W with a 10 kV high-voltage bias and a 27 mA emission current. A double pass cylindrical mirror energy analyzer (PHI model 15-255G) was used to detect the photoelectrons emitted from the sample surface.

To characterize the crystal structure and the size of synthesized films, X-ray diffraction (XRD) and glancing incidence X-ray diffraction (GIXRD) were carried out using a PANalytical X'Pert Pro diffractometer. The Cu Kα X-ray source used had a wavelength 1.5405 Å. A point detector with a 0.013° scanning step size and a 0.25 s counting time at each step was used to collect the X-ray diffraction theta-2theta (θ−2θ) scans. During the GIXRD scan, the glancing incident angle, ω was fixed at 1.5° while 2θ was varied. The detector scanned over 2θ in the scattering plane containing the incident X-ray and the surface normal, while the source and sample stage were fixed. XRD pole figures were collected using a Bruker D8 Discover X-ray diffractometer (also Cu Kα, λ = 1.5405 Å) with a point detector. The incident beam, detector, and antiscatter slits used had widths 0.2 mm, 0.6 mm, and 0.1 mm, respectively, with the exception of those used in the collection of the SnS_2(011) pole figure, which was taken with each slit of width 0.6 mm to improve the relatively weak signal-to-noise level. Each scan was completed in continuous scanning mode with 2° step sizes in both chi (χ) and phi (φ), and a 4 s counting time. The focused ion beam (FIB) in situ lift-out specimen preparation technique has been used to produce the TEM sample. TEM bright field images, high resolution images, and electron diffraction patterns were collected using JEOL 2100 F with a 200 keV energy electron beam. The electron gun (model RDA-003G) used in RHEED generated a 15 keV electron beam incident at a glancing angle of <1° on the sample surface and the emission current was 34 mA. The RHEED pattern was projected on a phosphor screen mounted on a 6-in. flange in a vacuum chamber (10^{-8} Torr) and was captured by a charge coupled device (CCD) camera positioned outside the chamber.

Vibrational modes were identified from Raman spectra collected using a Witec Alpha 300 confocal Raman microscope. The laser wavelength and power used were 532.1 nm and 17 mW, respectively. A 100× objective lens produced a spot size of ∼721 nm (= 1.22 × wavelength/numerical aperture of 0.9 for the 100× objective lens). The spectral resolution and step size used in Raman scattering data collection were each 0.02 cm^{-1}. The time-resolved photoluminescence (TRPL) measurement was performed via a customized TRPL system. A picosecond pulsed diode laser (Picoquant) with 405 nm wavelength was used as the excitation source. The pulse width and pulse frequency were 50 ps and 20 MHz, respectively. The estimated power density was ∼0.3 MW/cm^2 using a 1 μm laser spot size. The incident laser was directed onto the SnS_2 sample through an inverted microscope (Nikon Eclipse Ti). The luminescence signal was then directed into a monochromator (Princeton Instruments SP-2358), inside which the grating wavelength was fixed at the PL peak position. The scanning resolution of the momochromater was 0.001 nm, and the slit width was fixed to <2 mm. A single photon detector (Picoquant PDM) was aligned at the exit port of the monochromator to count photons, collect steady state PL and TRPL data of a 1 ns time resolution.

3. RESULTS

3.1. Morphology and Chemical Composition of Flakes. Figure 1c shows an SEM image from synthesized sample 1. There are isolated flakes with various tilt angles between 0° and 90° relative to the SiO_2 surface. The lateral size of each flake is in the range of tens of microns. Figure 1d shows an SEM (left) and an optical (right) top-view images of a flake with straight edges lying down on the substrate surface. The lateral size of our flakes ranges from 40 to 70 μm. It will be presented in later sections that these large size flakes are single crystals. Single crystals lack grain boundaries and have fewer defects that hinder carrier transport. Large lateral size in tens of microns is useful for optical measurement with the size of the probing incident light on the order of a micron and is also useful for fabricating an optoelectronic test device. The lateral size of SnS_2 crystal depends on growth methods. SnS_2 made from wet chemistry and hydrothermal are typically in the form of nanoparticles with a size less than 10 nm[21] or nanoflakes with a size around 100 nm.[20] CVD using SnO_2 nanowire and sulfur produces a few micrometer large nanosheets.[28] An atmospheric pressure CVD method using sulfur and SnS_2 powders produces a hexagonal shape SnS_2 crystal of size ranging from 13 to 43 μm.[15] Chemical vapor deposition using sulfur and SnO_2 produces 20−50 μm size SnS_2 crystals,[7] or several tens of microns crystal.[27] Our growth technique provides an additional and simple method to grow large size SnS_2 single crystals. The shape of the flake is half a hexagon with its longer edge contacting the substrate. Figure 1e shows a ∼90° tilted single flake of about 150 nm in thickness. Later X-ray pole figure analysis will provide quantitative values for the flakes' tilt angles. Electron energy dispersion spectra (EDS) were taken from one flake as shown in Figure 1d as well as in the areas between flakes. The EDS spectrum of the flake shown in Figure 1d reveals amounts of Sn, S, Si, and O. The Si and O signals come from the area underneath the flake because the probing depth of EDS is larger than the thickness of the flake. The atomic percentage ratio of S to Sn from the flake is about

DOI: 10.1021/acs.cgd.5b01512
Cryst. Growth Des. XXXX, XXX, XXX−XXX

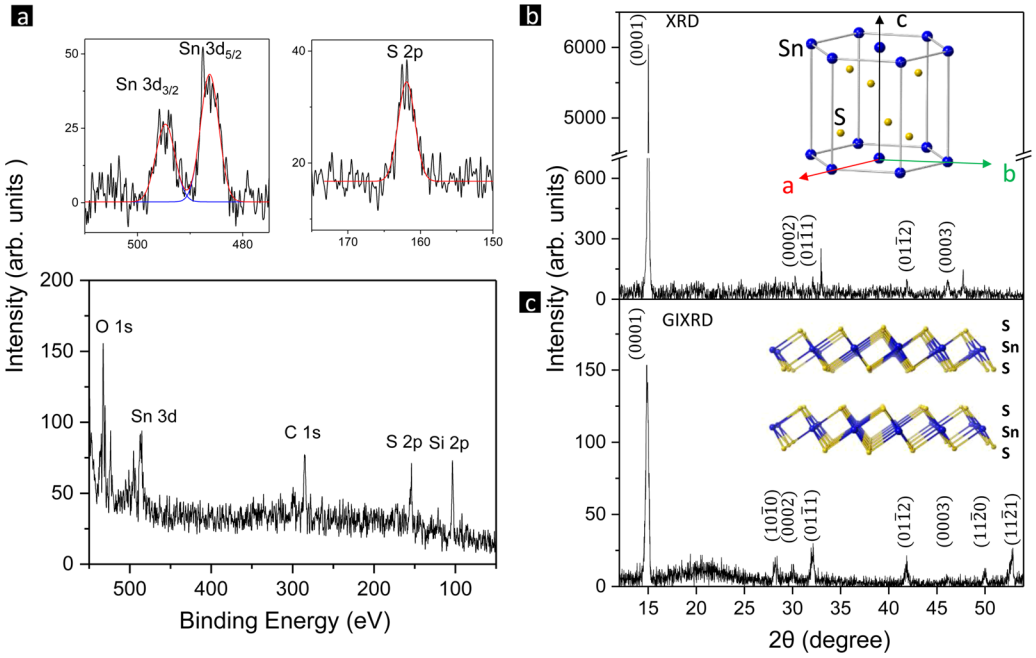

Figure 2. (a) X-ray photoelectron spectroscopy spectrum of the synthesized SnS_2 flakes. The upper left and upper right insets show Sn 3d spin−orbit splitting and S 2p, respectively. The Sn peaks were fit using two Gaussian curves (red curves) and the S peak was fit using one Gaussian. O 1s, C 1s, and Si 2p peaks are also observed from the SiO_2 substrate not covered by flakes. (b) X-ray diffraction and (c) grazing angle incidence X-ray diffraction theta vs two theta scans from the synthesized SnS_2 flakes. The inset in (b) is a ball model of the SnS_2 unit cell. The gold and blue spheres represent S and Sn atoms, respectively. The *c*-axis is the [0001] direction, and **a** and **b** are unit vectors 120° apart in the plane of the hexagon. The inset in (c) is a side-view of two monolayers of SnS_2.

2.05, slightly sulfur rich. The flat areas between flakes show no signals due to Sn or S but only Si, O, and C signals from the substrate. Figure 1f shows a TEM image of FIB-thinned single flake with three regions labeled as edge (E), inside (I), and further inside (FI).

The near surface chemical composition was cross checked by XPS and is shown in Figure 2a. In addition to Sn and S peaks, the Si, O, and C peaks are also observed. Although the number density of flakes on SiO_2 substrate is not high, XPS can still detect the Sn $3d_{3/2}$ and Sn $3d_{5/2}$ peaks as well as the S 2p peak. Their measured binding energies are 494.7, 486.2, and 161.9 eV, respectively. The spin−orbit splitting is ~8.5 eV. Our measured binding energies are consistent with 495.0 (Sn $3d_{3/2}$), 486.6 (Sn $3d_{5/2}$), and 161.6 eV (S $2p_{3/2}$) observed in SnS_2 film grown by atomic layer deposition[24] and 494.2, 485.7, and 161.6 eV observed in SnS_2 nanosheets grown by solvothermal methods.[25] Comparing our measured Sn $3d_{5/2}$ peak at 486.2 eV from SnS_2 flakes with the Sn $3d_{5/2}$ peak of pure Sn at 484.6 eV the Sn in SnS_2 has a chemical shift of 1.6 eV to a higher value from that of the pure Sn. Comparing the measured S 2p peak at 161.9 eV from SnS_2 flakes with the S 2p peak of pure S at 164.1 eV,[30] the S in SnS_2 has a chemical shift of 2.2 eV to a lower value from that of the pure S. This opposite chemical shifts are consistent with the electron transfers from Sn to S and forms chemical bonds between Sn and S. The XPS composition analysis reveals a Sn to S ratio in the SnS_2 flakes of 1 to 2.37. The relative amount of sulfur to Sn is higher than that obtained from a single flake using EDX. This is because the XPS beam covers a surface area much larger than that analyzed by EDX and detects signals from many flakes that may have various Sn to sulfur ratios on the SiO_2 substrate. In addition, the O 1s and Si 2p peaks are observed from the SiO_2 substrate.

3.2. Crystal Structure and Crystalline Size of Flakes.

The synthesized films were characterized by X-ray diffraction (XRD) and glancing incidence X-ray diffraction (GIXRD). Figure 2b,c shows XRD and GIXRD θ vs 2θ scans, respectively, measured from the same film synthesized on the SiO_2/Si substrate. The XRD scan shows a dominant peak at 2θ = 15.01°. This peak is consistent with the (0001) peak from hexagonal SnS_2 ($\alpha = \beta = 90°$, $\gamma = 120°$) with bulk lattice constants of a = 0.3645 nm, b = 0.3645 nm, and c = 0.5891 nm. This belongs to the $p\bar{3}m1$ space group (number 164), with ICSD number 042566. The GIXRD scan shows not only a dominant peak at 14.83° but also many small peaks, for example, at 32.04° and 41.88°. These peaks are consistent with the (0001), (01$\bar{1}$1), and (01$\bar{1}$2) peaks of 2H hexagonal SnS_2 (unit cell shown in the inset in Figure 2b). The unit cell consists of Sn atoms in a basal plane sandwiched between two layers of chalcogen S atoms. Note the S atoms do not line up in the *c*-direction. The Sn atom is octahedrally coordinated with the S atoms; i.e., one Sn atom bonds to six S atoms. The trilayer of SnS_2 can exist in polytypes where the stacking sequence of trilayer differs, such as 2H or 4H. For 2H type the stacking sequence is ···S−Sn−S, S−Sn−S··· See the inset of a side view of 2H structure in the GIXRD spectrum shown in Figure 2b. We need not consider the 4H structure because a (01$\bar{1}$3) peak at 34.66° for the 4H structure was not observed. Therefore, our sample is consistent with the 2H structure. The 2H unit length in the [0001] direction is also supported by AFM analysis to be presented later.

The average SnS_2 crystalline size D normal to the flakes (or flake thickness) can be estimated from Scherrer's formula: $D = \frac{K\lambda}{\beta \cos\theta}$, where K = 0.89 is the shape factor, λ is the X-ray wavelength of X-ray radiation, and β is the experimental full-width-at-half-maximum (fwhm) of the respective (*hkil*)

DOI: 10.1021/acs.cgd.5b01512
Cryst. Growth Des. XXXX, XXX, XXX−XXX

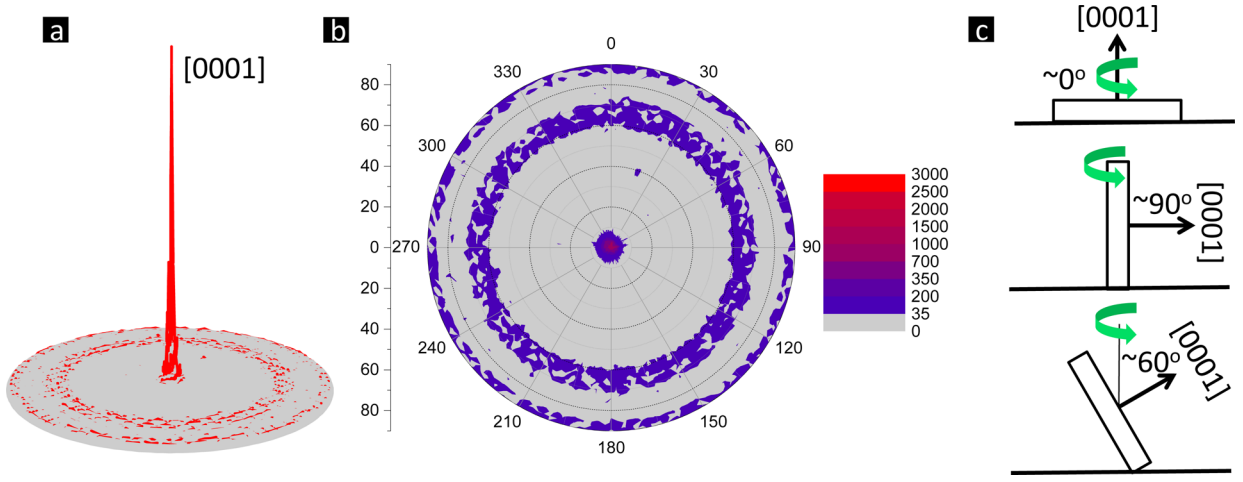

Figure 3. X-ray (0001) pole figure with intensity displayed in (a) 3D and (b) 2D. (c) Schematics of a lying down flake with [0001] parallel to the substrate normal, ~90° tilted flake, and ~60° tilted flake.

diffraction peak in units of radians. The average size (thickness) estimated from the fwhm of the (0001) peak from the XRD spectrum is 90.4 ± 1.63 nm. Note this number is an average from all flakes lying parallel to the substrate surface with the [0001] orientation normal to the substrate.

3.3. Texture of Flakes Measured by X-ray (0001) Pole Figures. Figure 3a shows a 3D plot of the (0001) X-ray pole figure measured by setting the two theta angle to 15.017° and running from 0° to 90° in chi. The center of the pole figure (chi angle near 0°) has a strong intensity implying that the majority of flakes lie parallel to the substrate. Figure 3b plots the 2D projection of the (0001) pole figure. Two rings of weaker intensity are observed at chi angles between 60° and 70° and between 85° and 90°. The center (0001) pole with high intensity is from the flakes lying parallel to the substrate (see the top schematic in Figure 3c). This is consistent with the (0001) peak observed in the XRD scan. The additional rings observed at chi angles of ~60° and ~90° imply that some flakes have their [0001] surface normals tilted away from the substrate normal by these angles. A flake with [0001] tilted 90° from the substrate normal is shown as in the middle schematic in Figure 3c. The ring close to a chi angle of 90° is produced by these flakes. The ring at chi angles between 60° and 70° corresponds to the [0001] direction of flakes being tilted between 60° and 70° away from substrate normal. This is shown as the bottom schematic in Figure 3c.

3.4. Symmetry of Flakes Measured by RHEED. RHEED patterns were collected at many in-plane azimuthal angles. At some azimuthal angles, clear, sharp diffraction spots were seen. Figure 4a,b shows two patterns at two azimuthal angles 15° apart. The scale bar in units of inverse angstroms ($Å^{-1}$) is shown. This scale bar was calibrated from a RHEED pattern of a single crystal CdTe film with a known lattice constant of 6.48 Å.[31] Note that the electron beam was incident perpendicular to the phosphor screen. The yellow-shaded scattering plane consists of incident wave vector k_{in} and outgoing wave vector k_{out} as shown in Figure 4. Discrete spots fill up the entire screen above the shadowing edge (denoted as a white dashed line). These spots satisfy the Laue condition $\Delta\mathbf{k} = \mathbf{G}(hkil)$, where $\Delta\mathbf{k}$ is the change in momentum and $\mathbf{G}(hkil)$ is a reciprocal lattice vector. To illustrate the symmetry among the spots, two reciprocal vectors are drawn as white arrows. The angle between the two white arrows ~ 120°. This symmetry is consistent with a hexagonal lattice with the electron beam incident along the [0001] or **c** direction and perpendicular to **a** and **b** directions in the plane of a flake. In both Figure 4a,b, the reciprocal lattice of SnS_2 are outlined as blue dashed lines with red dots. The diffraction pattern is the intersection of the Ewald sphere and the SnS_2 reciprocal lattice shown as red dots. Because of the 3-fold symmetry, we use a hexagonal coordinate system with the L axis lying along the [0001] direction and the $H-K$ plane perpendicular to it. A yellow arrow represents the reciprocal lattice distance G between the $(h0i0)$ family of planes, where $i = -(h + k)$. Using the reference scale bar, the measured reciprocal lattice distance $G \approx 0.318 \pm 0.002$ $Å^{-1}$. This measured reciprocal spacing is equal to the inverse of the interplanar spacing d_{h0i0}. Therefore, the measured $d_{h0i0} \approx 3.14 \pm 0.02$ Å. Because the angle between vectors **a** and **b** in a hexagonal lattice is not 90° but 120°, the relationship between d_{h0i0} and the real space lattice constant a is $\frac{1}{d_{hkil}^2} = \frac{4}{3}\left(\frac{h^2+hk+l^2}{a^2}\right) + \frac{l^2}{c^2}$. From this we have $d_{h0i0} = \frac{\sqrt{3}}{2h}a$. Using the measured $d_{10\bar{1}0}$, we obtain the lattice constant $a = 3.62 \pm 0.02$ Å. Similarly the lattice constant b can be obtained from the measured d_{0ki0} to be b = 3.62 ± 0.02 Å. These are comparable to the bulk lattice constants $a = b = 3.645$ Å. Because the electron beam is incident parallel to the [0001] direction, all diffraction spots have indices $(hki0)$. One cannot obtain the lattice constant c under this incident beam condition. However, the lattice constant $c = 5.89$ Å has already been obtained from the measured (0001) peak position of 15.01° in the X-ray θ vs 2θ scan. The bulk lattice constant $c = 5.891$ Å.

RHEED is a surface-sensitive analytical technique; for 15 keV electrons the electron mean free path is between 2 to 7 nm. The flake thickness estimated from the SEM image is in the range of 100 nm which is much thicker than the electron mean free path. The fact that we can observe RHEED transmission patterns implies that each pattern was obtained from the tapered thin top or edge part of a flake. This is supported by taking the inverse of the measured FWHMs of the $(h0i0)$ spots in the radial direction, which indicates a penetration length of about a few nanometers. The pattern in Figure 4a shows that the flake is standing up. The reciprocal lattice vector **G** (yellow arrow) along the direction of the row of $(h0i0)$ spots is rotated clockwise from the vertical direction of the RHEED pattern (the direction perpendicular to the shadowing edge) by an

DOI: 10.1021/acs.cgd.5b01512
Cryst. Growth Des. XXXX, XXX, XXX−XXX

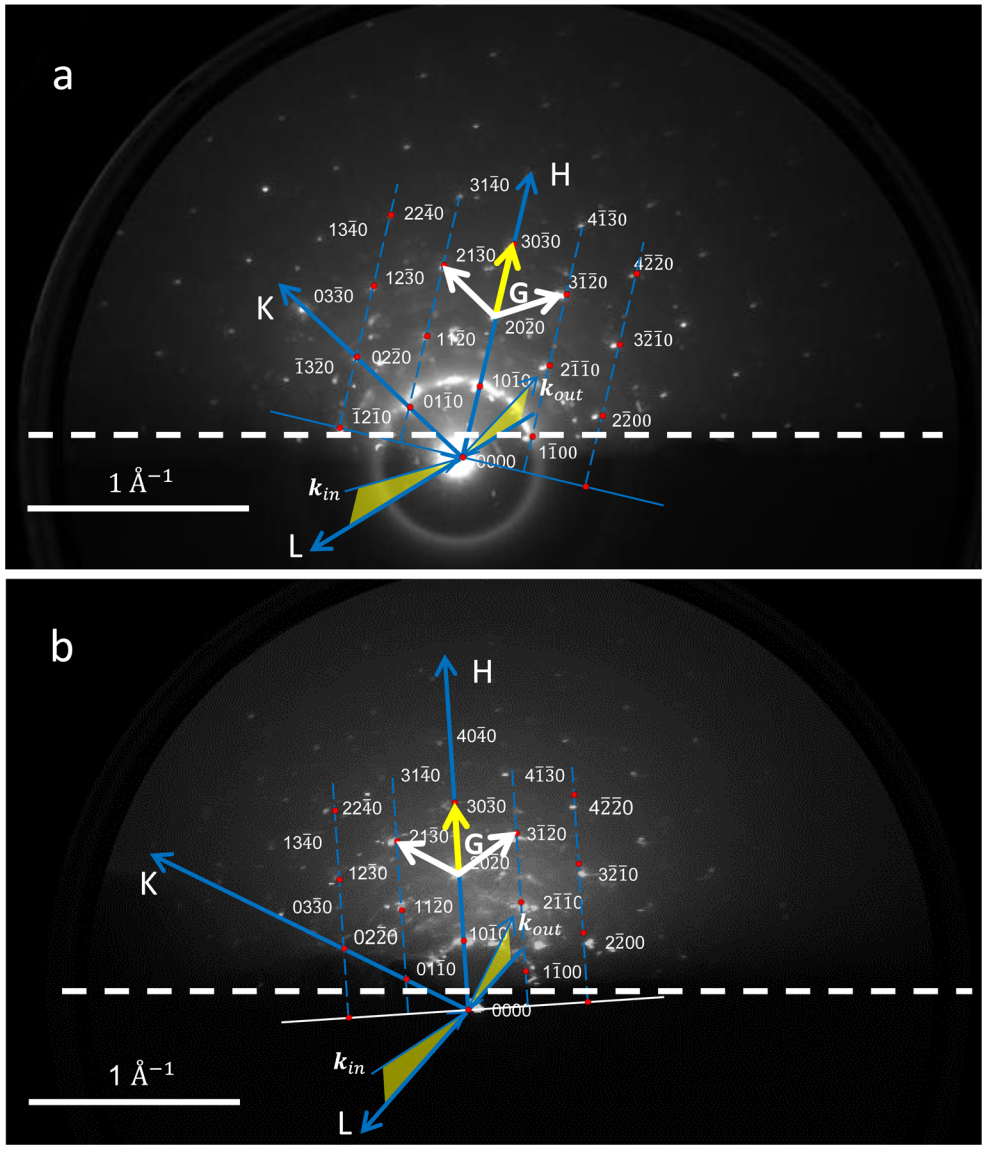

Figure 4. Reflection high energy electron diffraction patterns using a 15 keV electron beam taken at (a) azimuthal angle ϕ = 35° and (b) ϕ = 20°. The nearest **G**(*hkil*) of the SnS_2 pattern are shown as yellow and white arrows. Miller indices (*hkil*) of the diffraction spots are labeled. The shadowing edge is indicated as a white dashed line. Schematics of the scattering geometry of the electron beam and the reciprocal lattice of SnS_2 (blue dashed lines and red dots) from a vertically standing flake with its [0001] direction parallel to the substrate are drawn in both (a) and (b). *H*, *K*, and *L* are the axes of the hexagonal coordinate system. The *L* axis lies along the [0001] direction and the *H* axis makes a 14° angle to the right in (a) and a 5° angle to the left in (b) with respect to the direction perpendicular to the shadowing edge. The reciprocal lattice of SnS_2 representing by blue dashed lines and red dots are deliberately off a little to the sides of RHEED diffraction spots.

angle of ~14° for the upper pattern. At a different azimuthal angle, shown in the bottom panel of Figure 4b, **G** is rotated ~5° counterclockwise from the vertical direction. This observation is consistent with various morphological orientations of flakes and the fact that the top edges of flakes are not all parallel to each other as observed by SEM images.

The majority of flakes have [0001] perpendicular to the substrate as shown by X-ray pole figure analysis. The RHEED transmission patterns shown in Figure 4 are from flakes with the [0001] parallel to the substrate or standing vertically. No RHEED transmission pattern is observed from the flakes that lie parallel to the substrate. In addition, because of the random in-plane orientation, no clear reflection mode of RHEED pattern is observed.

Despite the low density of flakes on the SiO_2 surface, the RHEED patterns were observed because of the strong scattering cross section of electrons with the ion cores in the flakes. XRD and RHEED analyses show that the crystal structure of SnS_2 is close to that of the bulk, and the EDS and XPS spectra show that the Sn to S ratio is close to the stoichiometric ratio of 1:2. This implies that there is negligible chemical reaction between SnS_2 and the SiO_2 substrate.

The hexagonal symmetry observed in the RHEED patterns is consistent with low energy electron diffraction (LEED) pattern from molecular beam epitaxy grown SnS_2 overlayer on mica substrates reported in the literature.[32] Only one hexagonal pattern was seen on a phosphor screen due to the normal incidence of the electrons on the mica surface in LEED. In our RHEED patterns, many higher order *hkil* spots within the hexagonal symmetry were seen because the wave vector *k* for 15 keV in RHEED is 1 order of magnitude longer than *k* for

DOI: 10.1021/acs.cgd.5b01512
Cryst. Growth Des. XXXX, XXX, XXX−XXX

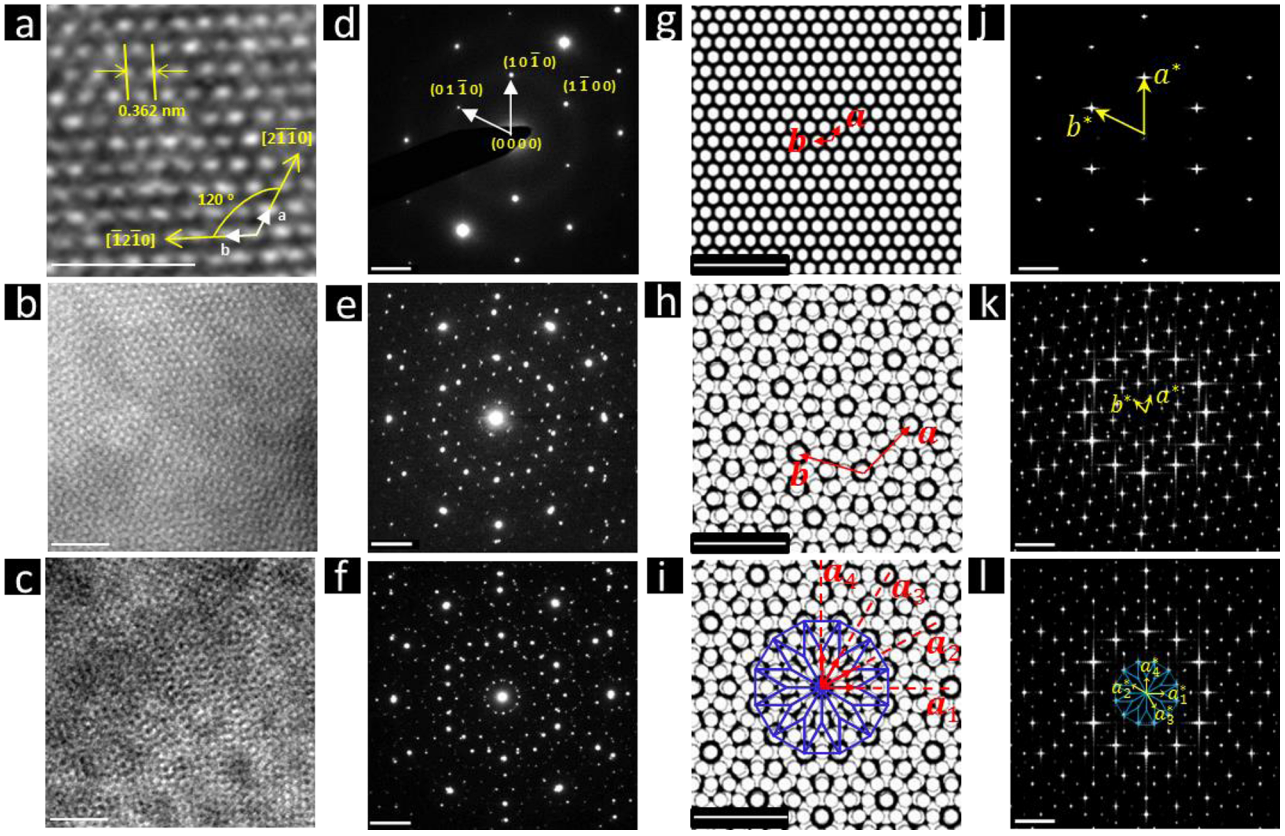

Figure 5. High resolution TEM images of a single SnS_2 flake taken at various locations: (a) edge, (b) inside, and (c) further inside. Note the size of scale bar changes from 2 nm in (a) to 10 nm in (b) and (c). The unit vectors **a** and **b** are labeled in (a). The corresponding TEM diffraction patterns are shown in (d), (e), and (f). The reciprocal unit vectors **a*** and **b*** are labeled in (d). The diffraction intensities in (e) and (f) have been enhanced for easy viewing. The scale bar in each is 2 nm^{-1}. Simulated overlapping hexagonal real space lattices with relative rotation of (g) 0°, (h) 28°, and (i) 30°, each with a 2 nm scale bar. The unit vectors **a** and **b** are labeled in (g) and (h). The quasi unit mesh with four unit vectors is labeled in (i). The corresponding fast Fourier transforms of (g), (h), and (i) are shown in (j), (k), and (l), respectively, each a 2 nm^{-1} scale bar. The reciprocal unit vectors **a*** and **b*** and quasi unit mesh are labeled in (j), (k), and (l).

150 eV in LEED (k ($Å^{-1}$) = $2\pi\sqrt{\frac{E(eV)}{150.4}}$). The longer wave vector allows the Ewald sphere to intercept more reciprocal lattice points which satisfy the Laue conditions. This allows us to determine the relative orientation of vectors **a** and **b** with respect to the substrate surface.

3.5. TEM Images and Diffraction Patterns of a Single SnS_2 Flake. *3.5.1. Images and Diffraction at Various Flake Thickness. Thinner Region near the Edge of a Flake.* Figure 5a,d shows a high resolution TEM (HRTEM) image and a selected area TEM diffraction pattern (DP), respectively, taken from the edge (E) that is the thinnest area of a FIB-thinned SnS_2 flake (see Figure 1f). The zone axis is along the [0001], or the **c** direction. Both the HRTEM image and DP show the hexagonal symmetry of a single domain. The unit vectors **a** and **b** are indicated as white arrows along the [$\bar{1}$2$\bar{1}$0] and [2$\bar{1}\bar{1}$0] directions (yellow arrows), respectively, in Figure 5a. The original HRTEM image size is much larger than that shown in Figure 5a which shows that the grain size is large and defects such as vacancies are hardly found.[33] Line scans of Figure 5a show the lattice spacing between adjacent lattice points along the [$\bar{1}$2$\bar{1}$0] is uniform with average measured spacing of a = 0.362 ± 0.010 nm. A similar value for b is obtained in the [2$\bar{1}\bar{1}$0] direction. To determine the unit lengths of **a** and **b** more accurately we analyzed the diffraction pattern in Figure 5d next. Miller indices of selected diffraction spots (0000), (01$\bar{1}$0), (10$\bar{1}$0), and (1$\bar{1}$00) are labeled.

The lengths of **G**($hkil$) in reciprocal space were measured from the (0000) spot to the six nearest neighbor spots in the DP shown in Figure 5d. The average value is G_{hkil} = 3.141 ± 0.002 nm^{-1}. This corresponds to a real space lattice constant of a = 0.367 ± 0.002 nm using the aforementioned equation for plane spacing in a hexagonal lattice. The lattice constant is consistent with the 2H structure of SnS_2 and is in reasonable agreement with the measured real space unit length shown in Figure 5a as well as the lattice constants obtained from XRD and RHEED. The fast Fourier transform (FFT) of the real space HRTEM image (from a much larger area) shown in Figure 5a using ImageJ software[34] gives the symmetry of a DP in agreement with the observed DP shown in Figure 5d.

Inside and Away from the Edge Region. Figure 5b,e shows an HRTEM image and a selected area TEM DP, respectively, of FIB-thinned SnS_2 flake, taken of the inside region away from the edge, labeled I in Figure 1f. This inside region is thicker than the edge region. The zone axis of the DP is along the [0001] direction. Comparing Figure 5b with Figure 5a, one can see a dramatic difference. Figure 5b appears to have a Moire pattern over the entire image area. Comparing Figure 5e with Figure 5d, one can see additional superlattice spots in addition to the basic spots seen in Figure 5(d). The six innermost spots (6-fold symmetry) around the center (0000) spot are rotated

DOI: 10.1021/acs.cgd.5b01512
Cryst. Growth Des. XXXX, XXX, XXX−XXX

15° clockwise from the vertical axis passing through the (0000) spot. The shortest superlattice distance in Figure 5e is about 0.27 of the unit reciprocal lattice distance of 3.141 ± 0.002 nm^{-1} shown in Figure 5d. A simulation to be presented later will show that these additional spots are a result of the Moire fringes observed in Figure 5b.

Further Inside Region. Figure 5c,f shows an HRTEM image and a selected area TEM DP, respectively, of FIB-thinned SnS_2 flake, taken in a region further inside the edge, indicated as FI in Figure 1f. This further inside region is even thicker than the inside region, which is thicker than the edge region. The zone axis of the DP is along the [0001] direction. Comparing Figure 5c with Figure 5a,b, one can see Figure 5c also appears to have a Moire pattern over the entire image area. Comparing the corresponding DP in Figure 5f with the DP shown in Figure 5e, one can see some differences. (1) The six innermost spots seen in Figure 5f are rotated 30° clockwise from the vertical axis passing through the (0000) spot instead of 15° clockwise shown in Figure 5e. (2) An additional six spots fill in between the six innermost spots just mentioned. In Figure 5f the total number of the innermost spots is 12 (12-fold symmetry). These innermost 12 spots align radially with the 12 spots in the concentric circles that contain the primary spots. (3) The DP is symmetric with respect to the vertical and horizontal directions passing through the (0000) spot. A simulation to be presented later will show that these additional spots are a result of the Moire pattern shown in Figure 5c. It appears that the order in the diffraction pattern can be described by a 12-fold symmetry observed in quasicrystals.

Moire fringes have been observed in homo- and hetero-epitaxial MX_2 systems. Examples of homoepitaxial systems are two overlapped grains of MoS_2 (examined by STEM-ADF),[35] MoS_2 crystals (examined by HRTEM),[36] and few-layered WS_2 transferred to a SiO_2/Si substrate (examined by HRTEM).[37] Examples of heteroepitaxial systems include vertical hetero-structures of five layers of MoS_2, WS_2, and WSe_2 on SnS_2 crystals (examined by TEM).[14] Moire fringes have also been observed in tri- and bilayer graphene (by DF-TEM),[38] graphene on hexgonal boron nitride (by STM)[39] and coalesced graphene grains on hexgonal boron nitride (by AFM).[40] For epitaxial WS_2 on lattice mismatched MoTe(0001), a Moire diffraction pattern with six salatellite spots around each integer spots were observed by low energy electron diffraction (LEED).[41]Our DP from single crystal SnS_2 layers clearly show superlattice satellite spots from Moire fringes that have a periodicity longer than the basic lattice constants.

3.5.2. Simulations of Moire Pattern and Diffraction Pattern. Moire fringes can be obtained by overlapping two hexagonal lattices and rotating one with respect to the other. Figure 5g–i shows one hexagonal lattice (representing Sn), two overlapping hexagonal lattices with a 28° intermediate rotation, and two overlapping hexagonal lattices with 30° intermediate rotation, respectively. After inverting the Moire patterns shown in Figure 5g–i via FFT using ImageJ, the corresponding simulated diffraction patterns are shown in Figure 5j–l, respectively. Every superlattice spot seen in the experimental diffraction patters shows up in the correct location in the FFT simulations, although the simulated intensities are more uniform than those observed. It should be noted that in order to compare simulated Moire patterns with the TEM DPs, the intensity in the TEM DPs shown in Figure 5e,f have been uniformly enhanced. The unit vectors **a** and **b** are labeled in Figure 5g,h. The superperiodicity with unit vectors **a** and **b** in Figure 5h spans a real space with lateral dimensions ~3.7 times larger than those of the real space spanned by the starting periodicity in Figure 5g. Taking the inverse of 3.7 gives ~0.27, which is consistent with the ratio of the superlattice reciprocal lengths in Figure 5k to the basic reciprocal lattice lengths labeled **a*** and **b*** in Figure 5j. The simulated DP shown in Figure 5k is rotated 15° clockwise from the vertical axis in agreement with the 15° clockwise rotation of unit vectors **a** and **b** in the Moire pattern shown in Figure 5h.

Figure 5l, the FFT of Figure 5i, shows sharp diffraction spots with a clear 12-fold symmetry, quite different from the superlattice symmetry shown in Figure 5k. It is well-known that such symmetry is forbidden in conventional crystals.[42] However, the 12-fold symmetry in quasicrystals was discovered by Ishimasa, Nissen and Fukano in intermetallic systems.[43−45] Stampfli−Gähler tiling is a well-established model to describe 12-fold symmetry structures.[46,47] We constructed a 12-fold dodecagon consisting of 12 equilateral triangles and 12 rhombi with an inclusion angle of 30°. Such dodecagons are the building blocks of the Stampfli−Gähler tiling. Although such a tiling structure lacks translational symmetry, it can still be indexed with integers, as for conventional crystals. However, instead of two base vectors, four must be used. The base vectors $\boldsymbol{a}_i$ (i = 1, 2, 3, and 4) in real space are labeled as four red arrows in Figure 5i. The corresponding reciprocal lattice in Figure 5l also exhibits 12-fold symmetry. In a similar way, we constructed a representation of the reciprocal lattice with 12 equilateral triangles and 12 rhombi. The corresponding reciprocal pseudo unit cell is drawn in Figure 5l in cyan. The corresponding four reciprocal basic vectors $\boldsymbol{a}_i^*$(i = 1,2,3 and 4) in the reciprocal space are also shown in Figure Figure 5l. The length, a of the sides of each equilateral triangle in Figure 5I is 0.71 nm, and the length a^* of the sides of each equilateral triangle in Figure 5l is 0.82 nm^{-1}. The relation between a and a^* follows: $a^* = \frac{1}{\sqrt{3}a}$.[48]

The sulfur to sulfur interaction between consecutive SnS_2 layers is of the weak van der Waals type. Thus, the rotation between layers during growth is possible. This happens frequently during the growth of the layered materials in both homo-[35−37] and heteroepitaxial systems[14] as mentioned previously. In the case of bilayer graphene the calculated torque per atom (proportional to the deviation from the interlayer potential) is a minimum around 30°,[38] consistent with the observation. In our present case, it is remarkable that with a two degrees difference in relative rotation between SnS_2 layers, the diffraction pattern can change from a superlattice with long-range order to a 12-fold symmetry with rotational order but lack of translational periodicity. The origin behind the observed relative angles between the layers that gives rise to the Morie fringes is not clear at the present time.

3.6. Island Shapes on the Surface of Large Flakes. SEM images show that the large SnS_2 flakes (>10 μm) in Figure 1d,e are either hexagonal or half-hexagonal when grown at 600 °C and above. From XRD we know the out-of-plane direction of the flakes is [0001]. This (0001) plane has a closely packed hexagonal unit cell and has the highest possible density of bonds. At the highest growth temperature of 600 °C, mostly large flat half-hexagonal-shaped flakes were formed. This shape can be considered a near-equilibrium shape. When the 30 min coevaporation ends, the reduction in temperature not only reduces the adatom diffusion, but also decreases the evaporation rates of Sn and S, resulting in different feeding

DOI: 10.1021/acs.cgd.5b01512
Cryst. Growth Des. XXXX, XXX, XXX−XXX

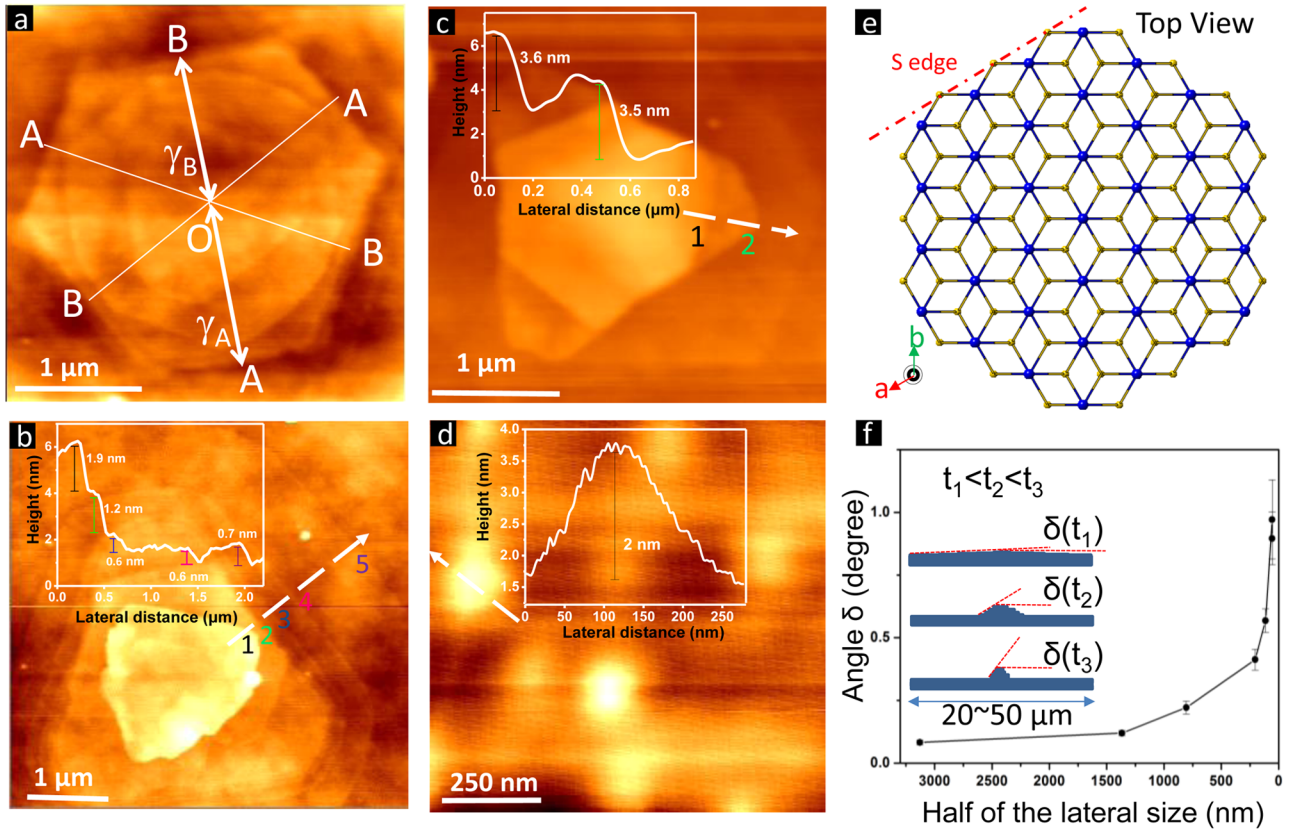

Figure 6. Atomic force microscopy images of multilayer islands on a large flake (>tens of μm): (a) a hexagonal island, (b–c) truncated triangular islands, and (d) a small island. The scale bars are 1 μm in (a–c) and 250 nm in (d). (e) A top-view schematic of a ball model of SnS_2 layers. The gold and blue spheres represent S and Sn atoms, respectively. The *c*-direction is perpendicular to the substrate. (f) Angular slope δ in units of degrees measured from multiple layer height islands as a function of half-lateral island size. Inset: A schematic of a possible growth process during cooling down. t_1 is an early time at 600 °C growth temperature and t_3 is a later time during the sample cooling down period (that is $t_3 > t_2 > t_1$).

rates of Sn and S to the growth of stochiometric SnS_2. Thus, smaller islands could form in nonequilibrium shapes, which are quenched during the cooling process. In optical images we observed smaller island features (<few microns size) on large flakes (>tens microns). One example is shown in Figure 1d in which the small islands are outlined by red circles. AFM was used to obtain better visual detail of these islands. Figure 6a–d shows AFM images of islands on the large flakes' surfaces with diameters ranging from a couple hundred nanometers to a couple microns. Islands with lateral dimensions of a couple μm are either hexagons or truncated triangles. Islands a couple hundred nm in diameter are more rounded, as in Figure 6d.

In general, the lateral size of each layer in these islands is smaller than that of the preceding layer. This implies there is a step edge barrier, E_{se}, that prevents the adatoms on the upper terrace from reaching the lower terrace and adding to the lateral dimension of the preceding layer. This can be qualitatively understood for the case in which an adatom moves toward a step where atoms have fewer nearest-neighbors. An atom being less bonded to the surface means a higher potential energy at the step. This potential barrier reduces the interlayer transport and biases the adatom diffusion away from the step edge.[49,50] Eventually a new island nucleates on the upper terrace, producing a multilayer structure. As mentioned previously, these islands are probably formed during the cooling period during which the thermal energy of adatoms cannot overcome the step edge barrier. In addition, during the cooling period the evaporation rates of Sn and S are also decreased, and thus fewer atoms reach the surfaces of the flakes. We will now discuss the observed island shape starting from the bottom layers to the multilayer regimes.

3.6.1. Shape of the Bottom Layers of an Island on a Large Flake. The shape of the bottom layers in each observed island shown in Figure 6a–c is hexagonal with six step edges and an angle between any two adjacent step edges of ~120°. Figure 6e shows the top view of a ball model of the (0001) plane of layered SnS_2. A hexagonal SnS_2 layer has six identical edges and these edges can be either Sn Zigzag (Sn-zz) terminations or S zigzag (S-zigzag) terminations. If these six edges have equal growth rates under equilibrium conditions, they tend to form hexagonal shapes. However, upon closer examination of the largest hexagonal island shown in Figure 6a, we found its six edges have slightly different lengths. Similar unequal step edge lengths are also observed in the bottom layers of the hexagonally shaped islands shown in Figure 6b,c. The inequality of island edge lengths has been reported for Pt islands grown by MBE on Pt(111) substrates at close to equilibrium temperatures ranging from 700 to 900 K.[51] They attributed this to a difference in step edge energies. A γ-plot was used to quantify the ratio of step edge energies in Pt islands as a result of different microfacets. Following a similar strategy, we've drawn a vector from the center of an island labeled O and perpendicular to a short step edge, A, (or long step edge, B) and named the length γ_A (or γ_B). The ratios of γ_B/γ_A along the three white outlines in Figure 6a are 0.88, 0.88, and 0.93. This ratio implies that the longer step edge B has lower step energy

DOI: 10.1021/acs.cgd.5b01512
Cryst. Growth Des. XXXX, XXX, XXX–XXX

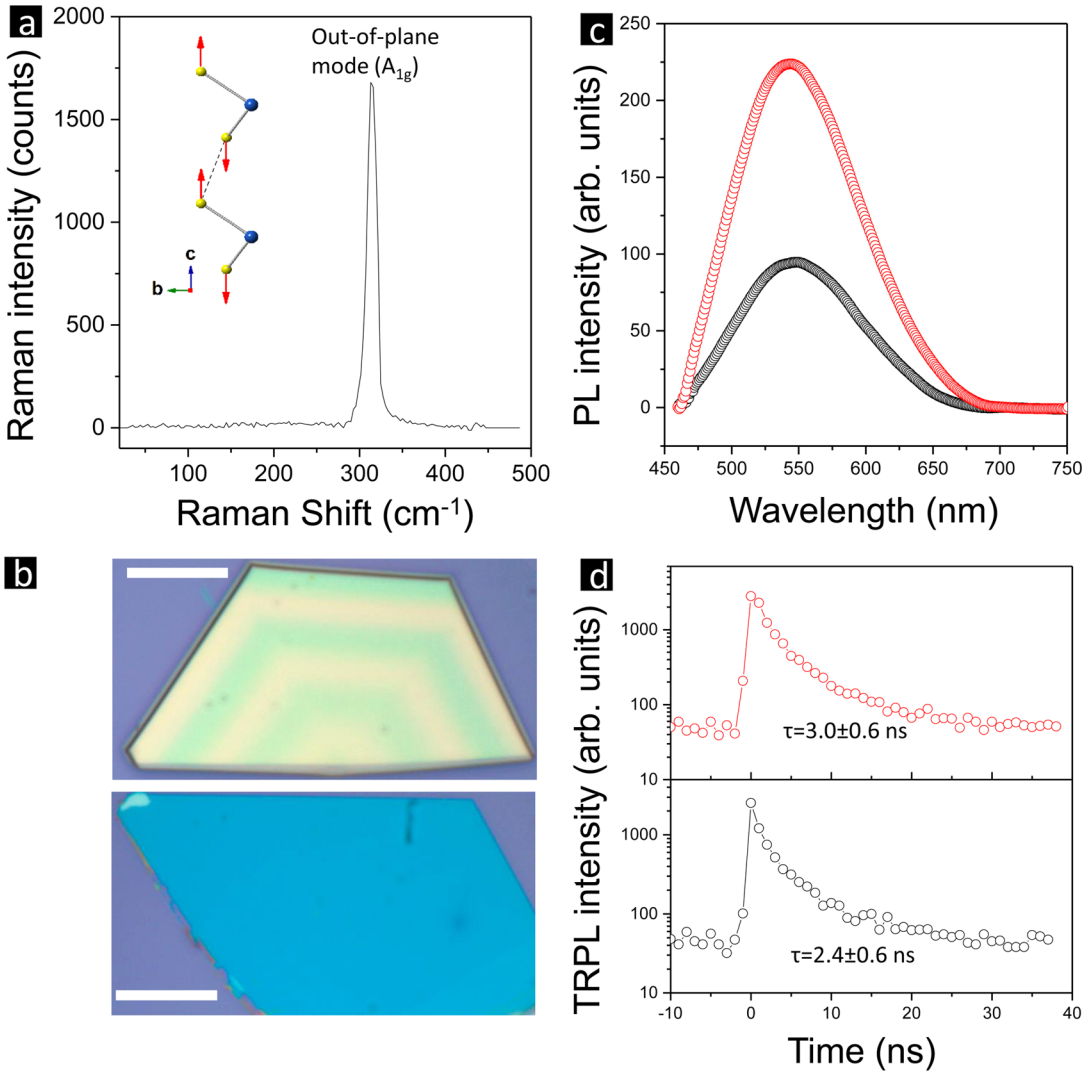

Figure 7. (a) Raman spectrum of a single SnS_2 flake. The vibrational mode A_{1g} is shown as an inset. The gold and blue spheres represent S and Sn atoms, respectively. The **c**-direction is perpendicular to the substrate. (b) Optical images of a single thicker flake (top) and a single thinner flake (bottom). Each scale bar is 10 μm. (c) Photoluminescence spectra corresponding to the thicker (red curve) and thinner flakes (black curve) shown in (b). (d) Time resolved PL of the thicker (red curve) and thinner (black curve) flakes with the corresponding carrier lifetime indicated.

than the short step edge, A. (These ratios are close to the step energy ratio of 0.87 ± 0.02 observed in Pt islands grown by MBE on Pt(111) substrate.[51])

The fact that we observe unequal step edge lengths implies that the six edges have unequal growth rates during the cooling period and that the edge structures may also differ. The unequal step edge lengths therefore likely result from kinetic limitations.

In our growth of SnS_2, we did not observe any triangular large flakes or smaller islands. This is unlike the triangular shape exhibited by monolayer MoS_2 grown under specific CVD conditions.[11] This difference can be attributed to the fact that the step edge terminations in SnS_2 are different from those in MoS_2. For hexagonal MoS_2 layers, there are three Mo-zz edges and three S-zz edges. They are not identical to one another. Each Mo atom at the Mo-zz step edge bonds to four S atoms with two dangling or unsaturated bonds (Z_e/Z = 2/6). At the S-zz step edge, each S atom bonds to two Mo atoms, leaving one unsaturated bond (Z_e/Z = 1/3). This structural difference in edges results in different levels of chemical activity under different Mo:S ratios. If the ratio of Mo to S supplied during growth is 1:2, the growth rates of Mo- and S-terminated step edges are equal. If under either S rich (<1:2) or Mo rich (>1:2) conditions, the flake shape will be triangular with S or Mo termination, respectively. In our SnS_2 case we do not observe purely triangular monolayers, but some islands have truncated triangular shapes; see Figure 6b,c.

3.6.2. Multilayer Island on a Large Flake. Figure 6b shows an AFM top-view image of an island that has a wedding cake-like morphology. The insets in Figure 6b–d show AFM height scans across the regions indicated with dashed white lines. The scans show step-like variations in height, indicating the existence of multiple SnS_2 trilayers (S–Sn–S). The smallest step height observed is ~0.6 nm. This is consistent with the lattice constant (0.589 nm) of SnS_2 in the *c* direction (perpendicular to the surface) determined by XRD. Other height differences are approximately integer multiples of 0.6 nm. For the island shown in Figure 6b, the ratio of the sum of all step heights observed for the several trilayers (~5 nm) vs the total lateral distance spanned by the several terraces (~2000 nm) indicates that the island has a slope of less than ~0.15° (arc tan(5/2000)) at its edges. For the island shown in Figure

DOI: 10.1021/acs.cgd.5b01512
Cryst. Growth Des. XXXX, XXX, XXX–XXX

6c, the slopes measured across other step barriers are also a couple tenths of degrees.

Figure 6c shows an island containing a hexagonal layer on top of a truncated triangular layer. The intensity is brightest near step edges, indicating increases in vertical height just before steps (see the AFM line scan in the inset). This is a direct result of the step edge barrier at a step edge, which prevents adatoms on the top of steps from hopping down to the lower terraces.[49,50]

In addition to the step edge barrier there is also a kink barrier at each corner with even higher energy. This is because there are even fewer bonding neighbors for an atom at the corner where two step edges meet than for atoms not at the corner. This is seen, for example, in the left most corner of the bottom layer in Figure 6a. That flakes with diameters of tens of micrometers and islands with diameters of a couple of micrometers have very smooth edges means there is sufficient edge diffusion. Without edge diffusion the steps meander.[52] AFM images of SnS_2 films grown by molecular beam epitaxy (MBE) on single crystal layered materials such as $MoTe_2$ and mica show similar layer-by-layer growth followed by island formation due to the nucleation of adatoms on successive layers.[32]

Figure 6f shows the angle obtained from the slope of islands vs r (half of the lateral size of the bottom most layer of the island). The slope is determined from the ratio of the vertical height of the island to r. The angle increases rapidly from ~0.1° to ~1° as r decreases to less than ~500 nm. Islands of various sizes and with different slopes result from the time at which growth begins (see t_1, t_2, and t_3 labeled on Figure 1b). During initial growth, at a temperature of 600 °C the terrace widths and step edge lengths increase. This results in an increased terrace area, which allows more adatoms to land on each terrace. Adatoms are able to overcome the step edge barrier to the preceding layer. Therefore, the island grows laterally in the shape of a hexagon up to tens of micrometers across and the island slope, $\delta(t_1)$, is small. Cooling from the 600 °C growth temperature to room temperature takes about 120 min, during which time the evaporation rates of Sn and S decrease. Adatom diffusion thus decreases to the point at which they can no longer overcome step edge barriers. In addition, there are increasingly limited supplies of Sn and S to further grow the island. Therefore, the smaller islands exhibit larger slopes, $\delta(t_3)$, and no distinct hexagonal shape, as observed in AFM images.

3.7. Vibrational Modes of Flakes Determined by Raman Spectroscopy. Figure 7a shows the Raman shift spectrum SnS_2 for sample 1. There is one peak observed at 314.44 ± 0.14 cm^{-1} with a fwhm of 13.37 ± 0.32 cm^{-1}. Raman data analyzed from three synthesized films with (0001) orientations are listed in Table 1.

The observed Raman shifts vary by less than 2 cm^{-1} for the three samples. These numbers are consistent with previous results obtained for exfoliated SnS_2.[3] The Raman shift of 314.44 cm^{-1} for sample 1 is close to the A_{1g} mode peak observed for single crystal SnS_2 at approximately 315 cm^{-1}.[53] A_{1g} is a singly degenerate active mode in which the two S atoms displace out-of-phase with respect to each other parallel to the c-axis, while the Sn atom is stationary (see the inset in Figure 7a). Our observed peak is also close to the peak at 314 cm^{-1} observed for seeded crystal SnS_2.[7] The observed Raman peaks at 312.83 and 312.48 cm^{-1} for samples 2 and 3 are closer to the peaks at 313 cm^{-1} exhibited by microplates made from sulfurizing F-doped SnO_2[14] and 312 cm^{-1} for nanoflowers and nanoyarns made by a modified hydrothermal method.[17] Our observed peak is higher than the 311 cm^{-1} peak of nanosheets made hydrothermally,[18] the 311 cm^{-1} peak of SnS_2 nanoparticles,[26] and the 311 cm^{-1} peak of exfoliated nanoflakes made by soaking bulk SnS_2 in butyllithium.[9]

Table 1. Raman Peak Locations and Full-Widths-at-Half-Maxima

sample	Raman shift (cm^{-1})	fwhm (cm^{-1})
1	314.44 ± 0.14	13.37 ± 0.32
2	312.83 ± 0.19	21.96 ± 0.64
3	312.48 ± 0.24	21.36 ± 0.52

The position of Raman peak shift has been modeled using three force constants: intrasandwich metal−ligand (M-L) bond stretching, intrasandwich M-L-M bond bending, and intersandwich L-L bond stretching. A Raman shift of 322.6 cm^{-1} was calculated for the A_{1g} mode for SnS_2.[53] That this number is higher than experimental values may be due to the fact that long-range Coulomb forces between S atoms were not considered in the model.

We did not observe Raman peaks at 474, 632, or 774 cm^{-1} associated with SnO_2.[54] This implies negligible chemical reaction between SnS_2 and the SiO_2 substrate.

3.8. Optical Bandgap of Flakes from Photoluminescence Spectroscopy and Carrier Lifetime from Time-Resolved PL. Figure 7b shows optical images of two single flakes of thicknesses ~32 nm (top) and ~20 nm (bottom). Figure 7c shows PL spectra obtained for the two flakes, with the red and black spectra corresponding to the thicker and thinner flakes, respectively. Both flakes exhibit one PL peak centered at 549 ± 5 nm. The FWHMs of the PL profiles are ~103 ± 2 nm and 105 ± 3 nm for the thicker and thinner flakes, respectively. The PL intensity is thickness-dependent, showing a nearly 5-fold increase when the thickness of flake increases from ~20 nm to ~32 nm. This trend is similar to the observed thickness-dependent PL of exfoliated SnS_2 in the few ML regime.[3]

The measured PL peaks at 549 nm (~2.25 eV) are due to radiative recombination of electron−hole pairs and are consistent with numerous experimental results reported in the literature: the PL peak at 550 nm measured for SnS_2 nanoparticles made by wet chemistry,[21] the PL peak between 540 and 562 nm for SnS_2 microplates,[14] the bandgap of ~2.23 eV estimated from the intercept point of the optical absorption spectrum vs. photon energy for mechanically exfoliated SnS_2 flakes,[3] the bandgap of ~2.25 eV estimated for the optical transmission of SnS_2 nanocrystals made from chemical vapor transport.[55] Other PL peaks reported for nanostructured SnS_2 exhibit either a blue- or red-shift relative to ours at 549 nm. The blue-shift is due to confinement effects in SnS_2 nanoparticles[22] and the red-shift may stem from deep level emission from a stoichiometric variation in nanostructured SnS_2.[21−23,56] One calculated bandgap for single crystal SnS_2 using HSE06 techniques is 2.24 eV,[57] close to our experimental value. Our observed PL peaks as well as existing reports imply that SnS_2 flakes with more than one monolayer possess a direct bandgap.

Figure 7d shows TRPL spectra measured for the same two flakes at a fixed wavelength of 550 nm. The data points were fit by an exponential function to give carrier lifetimes of 3.0 ± 0.6 ns and 2.2 ± 0.6 ns for the thicker and thinner flakes, respectively. The measured lifetimes from our flakes are about 1 order of magnitude longer than the lifetime of 0.25 ns

DOI: 10.1021/acs.cgd.5b01512
Cryst. Growth Des. XXXX, XXX, XXX−XXX

measured for multilayer SnS_2.[3] Our observed ~3 ns carrier lifetime implies that the diffusion lengths of carriers in flakes may be very long. Considering the direct band gap nature of the SnS_2, thin film solar cells made of our materials suggest a promising opportunity.

4. CONCLUSION

We report a simple one step thermal coevaporation method for synthesizing ultrathin SnS_2 flakes with lateral sizes of over tens of microns. Each flake is a single crystal with 2H structure and (0001) orientation as determined by XRD, RHEED, and TEM. X-ray pole figure analysis shows that the majority of flakes lie parallel to the substrate, while some tilt ~60° or ~90° from the substrate normal. For a few-layer-thick flake, Moire fringes with 6-fold and 12-fold symmetries were observed by TEM. The corresponding TEM diffraction patterns are consistent with simulated Fourier transform Moire patterns from two layers of SnS_2 rotated at specific angles with respect to one another. The bulk and near surface composition ratios of Sn to S in the SnS_2 flakes are close to 1:2 as determined by EDX and XPS, respectively. AFM analysis of islands on the flakes including line scans, determination of step edge lengths and shapes of islands reveals the nucleation and growth of flakes with step edge barriers and a difference in step edge free energies based on the type of edge termination. Raman spectra show one A_{1g} mode at ~314 cm^{-1} with a narrow fwhm implying good local crystalline order. Photoluminescence spectra of flakes show one peak at ~549 nm. The observation of this PL peak location indicates an optical bandgap of ~2.25 eV. The measured time-resolved PL is slightly thickness-dependent ranging from 2 to 3 ns.

AUTHOR INFORMATION

Corresponding Author

*E-mail: yangy20@rpi.edu.

Notes

The authors declare no competing financial interest.

ACKNOWLEDGMENTS

This work is supported by the New York State Foundation of Science, Technology and Innovation (NYSTAR) through Focus Center-New York and Rensselaer. TEM studies were carried out in whole at the Center for Functional Nanomaterials, Brookhaven National Laboratory, which is operated by the U.S. department of Energy, Office of Basic Sciences, under contract no. DE-AC02-98CH10886. We thank W. Xie and Dustin Andersen for valuable discussions.

REFERENCES

(1) Splendiani, A.; Sun, L.; Zhang, Y.; Li, T.; Kim, J.; Chim, C.-Y.; Galli, G.; Wang, F. Emerging photoluminescence in monolayer MoS_2. *Nano Lett.* **2010**, *10* (4), 1271−1275.

(2) Radisavljevic, B.; Radenovic, A.; Brivio, J.; Giacometti, V.; Kis, A. Single-layer MoS_2 transistors. *Nat. Nanotechnol.* **2011**, *6*, 147−150.

(3) Huang, Y.; Sutter, E.; Sadowski, J. T.; Cotlet, M.; Monti, O. L. A.; Racke, D. A.; Neupane, M. R.; Wickramaratne, D.; Lake, R. K.; Parkinson, B. A.; Sutter, P. Tin disulfide - An emerging layered metal dichalcogesnide semiconductor: Materials properties and device characteristics. *ACS Nano* **2014**, *8* (10), 10743−10755.

(4) De, D.; Manongdo, J.; See, S.; Zhang, V.; Guloy, A.; Peng, H. High on/off ratio field effect transistors based on exfoliated crystalline SnS_2 nano-membranes. *Nanotechnology* **2013**, *24* (2), 025202−1−6.

(5) Song, H. S.; Li, S. L.; Gao, L.; Xu, Y.; Ueno, K.; Tang, J.; Cheng, Y. B.; Tsukagoshi, K. High-performance top-gated monolayer SnS_2 field effect transistors and their integrated logic circuits. *Nanoscale* **2013**, *5* (20), 9666−9670.

(6) Wu, Z.; Xue, Y.; Zhang, Y.; Li, J.; Chen, T. SnS_2 nanosheet-based microstructures with high adsorption capabilities and visible light photocatalytic activities. *RSC Adv.* **2015**, *5* (31), 24640−24648.

(7) Su, G.; Hadjiev, V. G.; Loya, P. E.; Zhang, J.; Lei, S.; Maharjan, S.; Dong, P.; Ajayan, P. M.; Lou, J.; Peng, H. Chemical Vapor Deposition of Thin Crystals of Layered Semiconductor SnS_2 for Fast Photodetection Application. *Nano Lett.* **2015**, *15* (1), 506−513.

(8) Tao, Y.; Wu, X.; Wang, W.; Wang, J. Flexible photodetector from ultraviolet to near infrared based on a SnS_2 nanosheet microsphere film. *J. Mater. Chem. C* **2015**, *3* (6), 1347−1353.

(9) Liu, Y.; Kang, H.; Jiao, L.; Chen, C.; Cao, K.; Wang, Y.; Yuan, H. Exfoliated-SnS_2 restacked on graphene as a high-capacity, high-rate, and long-cycle life anode for sodium ion batteries. *Nanoscale* **2015**, *7* (4), 1325−1332.

(10) Qu, B.; Ji, G.; Ding, B.; Lu, M.; Chen, W.; Lee, J. Y. Origin of the Increased Li^+-Storage Capacity of Stacked SnS_2/Graphene Nanocomposite. *ChemElectroChem* **2015**, *2* (8), 1138−1143.

(11) Wang, J.; Luo, C.; Mao, J.; Zhu, Y.; Fan, X.; Gao, T.; Mignerey, A. C.; Wang, C. Solid-State Fabrication of SnS_2/C Nanospheres for High-Performance Sodium Ion Battery Anode. *ACS Appl. Mater. Interfaces* **2015**, *7* (21), 11476−11481.

(12) Wang, G.; Peng, J.; Zhang, L.; Zhang, J.; Dai, B.; Zhu, M.; Xia, L.; Yu, F. Two-dimensional SnS_2@PANI nanoplates with high capacity and excellent stability for lithium-ion batteries. *J. Mater. Chem. A* **2015**, *3* (7), 3659−3666.

(13) Chang, K.; Wang, Z.; Huang, G.; Li, H.; Chen, W.; Lee, J. Y. Few-layer SnS_2/graphene hybrid with exceptional electrochemical performance as lithium-ion battery anode. *J. Power Sources* **2012**, *201*, 259−266.

(14) Zhang, X.; Meng, F.; Christianson, J. R.; Arroyo-Torres, C.; Lukowski, M. A.; Liang, D.; Schmidt, J. R.; Jin, S. Vertical Heterostructures of Layered Metal Chalcogenides by van der Waals Epitaxy. *Nano Lett.* **2014**, *14* (6), 3047−3054.

(15) Xia, J.; Zhu, D.; Wang, L.; Huang, B.; Huang, X.; Meng, X. M. Large-Scale Growth of Two-Dimensional SnS_2 Crystals Driven by Screw Dislocations and Application to Photodetectors. *Adv. Funct. Mater.* **2015**, *25* (27), 4255−4261.

(16) Joshi, P. D.; Joag, D. S.; Rout, C. S.; Late, D. J. Photosensitive field emission study of SnS_2 nanosheets. *J. Vac. Sci. Technol. B* **2015**, *33* (3), 03C106−1−4.

(17) Mondal, C.; Ganguly, M.; Pal, J.; Roy, A.; Jana, J.; Pal, T. Morphology controlled synthesis of SnS_2 nanomaterial for promoting photocatalytic reduction of aqueous Cr(VI) under visible light. *Langmuir* **2014**, *30* (14), 4157−4164.

(18) Rout, C. S.; Joshi, P. D.; Kashid, R. V.; Joag, D. S.; More, M. A.; Simbeck, A. J.; Washington, M.; Nayak, S. K.; Late, D. J. Enhanced field emission properties of doped graphene nanosheets with layered SnS_2. *Appl. Phys. Lett.* **2014**, *105* (4), 043109−1−5.

(19) Wang, C.; Tang, K.; Yang, Q.; Qian, Y. Raman scattering, far infrared spectrum and photoluminescence of SnS_2 nanocrystallites. *Chem. Phys. Lett.* **2002**, *357* (5−6), 371−375.

(20) Umar, A.; Akhtar, M. S.; Dar, G. N.; Abaker, M.; Al-Hajry, A.; Baskoutas, S. Visible-light-driven photocatalytic and chemical sensing properties of SnS_2 nanoflakes. *Talanta* **2013**, *114*, 183−190.

(21) Chaki, S. H.; Deshpande, M. P.; Trivedi, D. P.; Tailor, J. P.; Chaudhary, M. D.; Mahato, K. Wet chemical synthesis and characterization of SnS_2 nanoparticles. *Appl. Nanosci.* **2013**, *3* (3), 189−195.

(22) Kiruthigaa, G.; Manoharan, C.; Raju, C.; Jayabharathi, J.; Dhanapandian, S. Solid state synthesis and spectral investigations of nanostructure SnS_2. *Spectrochim. Acta, Part A* **2014**, *129*, 415−420.

(23) Manoharan, C.; Kiruthigaa, G.; Dhanapandian, S.; Kumar, K. S.; Jothibas, M., Preparation and characterization of nano structured SnS_2 by solid state reaction method. *Proceedings of the International Conference on Advanced Nanomaterials & Emerging Engineering Technologies* ICANMEET-2013, 2013; pp 30−33.

DOI: 10.1021/acs.cgd.5b01512
Cryst. Growth Des. XXXX, XXX, XXX−XXX

(24) Ham, G.; Shin, S.; Park, J.; Choi, H.; Kim, J.; Lee, Y.-A.; Seo, H.; Jeon, H. Tuning the Electronic Structure of Tin Sulfides Grown by Atomic Layer Deposition. *ACS Appl. Mater. Interfaces* **2013**, *5* (18), 8889−8896.
(25) Wei, R.; Hu, J.; Zhou, T.; Zhou, X.; Liu, J.; Li, J. Ultrathin SnS_2 nanosheets with exposed {001} facets and enhanced photocatalytic properties. *Acta Mater.* **2014**, *66*, 163−171.
(26) Méndez-López, A.; Morales-Acevedo, A.; Acosta-Silva, Y. d. J.; Katagiri, H.; Matsumoto, Y.; Zelaya-Angel, O.; Ortega-López, M. Study of the synthesis of self-assembled tin disulfide nanoparticles prepared by a low-cost process. *Phys. Status Solidi C* **2015**, *12* (6), 564−567.
(27) Ahn, J.-H.; Lee, M.-J.; Heo, H.; Sung, J. H.; Kim, K.; Hwang, H.; Jo, M.-H. Deterministic Two-Dimensional Polymorphism Growth of Hexagonal n-Type SnS_2 and Orthorhombic p-Type SnS Crystals. *Nano Lett.* **2015**, *15* (6), 3703−3708.
(28) Huang, Y.; Deng, H.-X.; Xu, K.; Wang, Z.-X.; Wang, Q.-S.; Wang, F.-M.; Wang, F.; Zhan, X.-Y.; Li, S.-S.; Luo, J.-W.; He, J. Highly sensitive and fast phototransistor based on large size CVD-grown SnS_2 nanosheets. *Nanoscale* **2015**, *7* (33), 14093−14099.
(29) Robles, V.; Trigo, J. F.; Guillén, C.; Herrero, J. SnS absorber thin films by co-evaporation: Optimization of the growth rate and influence of the annealing. *Thin Solid Films* **2015**, *582*, 249−252.
(30) Wagner, C. D.; Riggs, W. M.; Davis, L. E.; Moulder, J. F.; Muilenberg, G. E. *Handbook of X-ray Photoelectron Spectroscopy*; Perkin-Elmer Corporation: Waltham, MA, 1978.
(31) Chen, L.; Dash, J.; Su, P.; Lin, C. F.; Bhat, I.; Lu, T. M.; Wang, G. C. Instrument response of reflection high energy electron diffraction pole figure. *Appl. Surf. Sci.* **2014**, *288*, 458−465.
(32) Schlaf, R.; Louder, D.; Lang, O.; Pettenkofer, C.; Jaegermann, W.; Nebesny, K. W.; Lee, P. A.; Parkinson, B. A.; Armstrong, N. R. Molecular beam epitaxy growth of thin films of SnS_2 and $SnSe_2$ on cleaved mica and the basal planes of single-crystal layered semiconductors: Reflection high-energy electron diffraction, low-energy electron diffraction, photoemission, and scanning tunneling microscopy/atomic force microscopy characterization. *J. Vac. Sci. Technol., A* **1995**, *13* (3), 1761−1767.
(33) van der Zande, A. M.; Huang, P. Y.; Chenet, D. A.; Berkelbach, T. C.; You, Y.; Lee, G.-H.; Heinz, T. F.; Reichman, D. R.; Muller, D. A.; Hone, J. C. Grains and grain boundaries in highly crystalline monolayer molybdenum disulphide. *Nat. Mater.* **2013**, *12* (6), 554−561.
(34) Schneider, C. A.; Rasband, W. S.; Eliceiri, K. W. NIH Image to ImageJ: 25 years of image analysis. *Nat. Methods* **2012**, *9* (7), 671−675.
(35) Najmaei, S.; Liu, Z.; Zhou, W.; Zou, X.; Shi, G.; Lei, S.; Yakobson, B. I.; Idrobo, J.-C.; Ajayan, P. M.; Lou, J. Vapour phase growth and grain boundary structure of molybdenum disulphide atomic layers. *Nat. Mater.* **2013**, *12* (8), 754−759.
(36) Reyes-Gasga, J.; Tehuacanero, S.; Yacamán, M. J. Moiré patterns in high resolution electron microscopy images of MoS_2. *Microsc. Res. Tech.* **1998**, *40* (1), 2−9.
(37) Perea-López, N.; Elías, A. L.; Berkdemir, A.; Castro-Beltran, A.; Gutiérrez, H. R.; Feng, S.; Lv, R.; Hayashi, T.; López-Urías, F.; Ghosh, S.; Muchharla, B.; Talapatra, S.; Terrones, H.; Terrones, M. Photosensor Device Based on Few-Layered WS_2 Films. *Adv. Funct. Mater.* **2013**, *23* (44), 5511−5517.
(38) Brown, L.; Hovden, R.; Huang, P.; Wojcik, M.; Muller, D. A.; Park, J. Twinning and Twisting of Tri- and Bilayer Graphene. *Nano Lett.* **2012**, *12* (3), 1609−1615.
(39) Xue, J.; Sanchez-Yamagishi, J.; Bulmash, D.; Jacquod, P.; Deshpande, A.; Watanabe, K.; Taniguchi, T.; Jarillo-Herrero, P.; LeRoy, B. J. Scanning tunnelling microscopy and spectroscopy of ultra-flat graphene on hexagonal boron nitride. *Nat. Mater.* **2011**, *10* (4), 282−285.
(40) Yang, W.; Chen, G.; Shi, Z.; Liu, C.-C.; Zhang, L.; Xie, G.; Cheng, M.; Wang, D.; Yang, R.; Shi, D.; Watanabe, K.; Taniguchi, T.; Yao, Y.; Zhang, Y.; Zhang, G. Epitaxial growth of single-domain graphene on hexagonal boron nitride. *Nat. Mater.* **2013**, *12* (9), 792−797.
(41) Tiefenbacher, S.; Pettenkofer, C.; Jaegermann, W. Moiré pattern in LEED obtained by van der Waals epitaxy of lattice mismatched $WS_2/MoTe_2(0001)$ heterointerfaces. *Surf. Sci.* **2000**, *450* (3), 181−190.
(42) Bamberg, J.; Cairns, G.; Kilminster, D. The Crystallographic Restriction, Permutations, and Goldbach's Conjecture. *American Mathematical Monthly* **2003**, *110* (3), 202−209.
(43) Ishimasa, T.; Nissen, H. U.; Fukano, Y. New ordered state between crystalline and amorphous in Ni-Cr particles. *Phys. Rev. Lett.* **1985**, *55* (5), 511−513.
(44) Ishimasa, T.; Nissen, H.-U.; Fukano, Y. Electron microscopy of crystalloid structure in Ni-Cr small particles. *Philos. Mag. A* **1988**, *58* (6), 835−863.
(45) Beeli, C.; Gähler, F.; Nissen, H.-U.; Stadelmann, P. Comparison of HREM images and contrast simulations for dodecagonal Ni-Cr quasicrystals. *J. Phys. (Paris)* **1990**, *51* (7), 661−674.
(46) Stampfli, P. A Dodecagonal Quasi-periodic Lattice In 2 Dimensions. *Helvetica Phys. Acta* **1986**, *59* (6−7), 1260−1263.
(47) Gähler, F. *Crystallography of Dodecagonal Quasicrystals*; Universitätsbibliothek der Universität Stuttgart: Stuttgart, 2009.
(48) Yamamoto, A. Crystallography of quasiperiodic crystals. *Acta Crystallogr., Sect. A: Found. Crystallogr.* **1996**, *52* (4), 509−560.
(49) Ehrlich, G.; Hudda, F. G. Atomic View of Surface Self-Diffusion: Tungsten on Tungsten. *J. Chem. Phys.* **1966**, *44* (3), 1039−1049.
(50) Schwoebel, R. L.; Shipsey, E. J. Step Motion on Crystal Surfaces. *J. Appl. Phys.* **1966**, *37* (10), 3682−3686.
(51) Michely, T.; Comsa, G. *Morphological Organization in Epitaxial Growth and Removal* **1999**, *14*, 265−306.
(52) Ratsch, C.; Garcia, J.; Caflisch, R. E. Influence of edge diffusion on the growth mode on vicinal surfaces. *Appl. Phys. Lett.* **2005**, *87*, 141901−1−3.
(53) Smith, A. J.; Meek, P. E.; Liang, W. Y. Raman scattering studies of SnS_2 and $SnSe_2$. *J. Phys. C: Solid State Phys.* **1977**, *10* (8), 1321−1323.
(54) Sun, S. H.; Meng, G. W.; Zhang, G. X.; Gao, T.; Geng, B. Y.; Zhang, L. D.; Zuo, J. Raman scattering study of rutile SnO_2 nanobelts synthesized by thermal evaporation of Sn powders. *Chem. Phys. Lett.* **2003**, *376* (1−2), 103−107.
(55) Powell, M. J. The effect of pressure on the optical properties of 2H and 4H SnS_2. *J. Phys. C: Solid State Phys.* **1977**, *10*, 2967−2977.
(56) Deshpande, N. G.; Sagade, A. A.; Gudage, Y. G.; Lokhande, C. D.; Sharma, R. Growth and characterization of tin disulfide (SnS_2) thin film deposited by successive ionic layer adsorption and reaction (SILAR) technique. *J. Alloys Compd.* **2007**, *436* (1−2), 421−426.
(57) Burton, L. A.; Colombara, D.; Abellon, R. D.; Grozema, F. C.; Peter, L. M.; Savenije, T. J.; Dennler, G.; Walsh, A. Synthesis, Characterization, and Electronic Structure of Single-Crystal SnS, Sn_2S_3, and SnS_2. *Chem. Mater.* **2013**, *25* (24), 4908−4916.

DOI: 10.1021/acs.cgd.5b01512
Cryst. Growth Des. XXXX, XXX, XXX−XXX